PHYSICAL REVIEW D **74,** 034508 (2006)

Nucleon electromagnetic form factors from lattice QCD

C. Alexandrou,[1] G. Koutsou,[1] J. W. Negele,[2] and A. Tsapalis[3]

[1]*Department of Physics, University of Cyprus, CY-1678 Nicosia, Cyprus*

[2]*Center for Theoretical Physics, Laboratory for Nuclear Science and Department of Physics, Massachusetts Institute of Technology, Cambridge, Massachusetts 02139, USA*

[3]*Institute for Accelerating Systems and Applications, University of Athens, Athens, Greece*

(Received 18 May 2006; published 11 August 2006)

We evaluate the isovector nucleon electromagnetic form factors in quenched and unquenched QCD on the lattice using Wilson fermions. In the quenched theory we use a lattice of spatial size 3 fm at $\beta = 6.0$ enabling us to reach low momentum transfers and a lowest pion mass of about 400 MeV. In the unquenched theory we use two degenerate flavors of dynamical Wilson fermions on a lattice of spatial size 1.9 fm at $\beta = 5.6$ and lowest pion mass of about 380 MeV enabling comparison with the results obtained in the quenched theory. that unquenching effects are small for the pion masses considered in this work. We compare our lattice results to the isovector part of the experimentally measured form factors.

DOI: 10.1103/PhysRevD.74.034508 PACS numbers: 11.15.Ha, 12.38.−t, 12.38.Aw, 12.38.Gc

I. INTRODUCTION

The elastic nucleon electromagnetic form factors are fundamental quantities characterizing important features of neutron and proton structure that include their size, charge distribution and magnetization. An accurate determination of these quantities in lattice QCD is timely and important because of a new generation of precision experiments. In particular, polarization experiments [1] that measure directly the ratio of the proton electric to magnetic form factor, $\mu_p G_E^p/G_M^p$, have shown a qualitative different behavior than the traditional Rosenbluth separation. The ratio $\mu_p G_E^p/G_M^p$ instead of being approximately constant falls off almost linearly with the momentum transfer squared, q^2, which means that the electric form factor falls faster than the magnetic. Recent reviews on the experimental situation can be found in Refs. [2,3]. Precise lattice data for the nucleon form factors for large values of q^2 will enable comparison with experiment and could lead to an understanding of the approach to asymptotic scaling. Furthermore, access to low momentum transfers will enable a better determination of phenomenologically interesting quantities such as the root mean squared (r.m.s.) radius of the transverse quark distribution in the nucleon [4]. To access small momentum transfers we need a lattice with large spatial extent, L, since the smallest available momentum is $2\pi/L$. Although large momentum transfers are in principle available on typical lattices, the Fourier transform of two- and three-point functions becomes noise-dominated for momentum transfers beyond about 2 GeV^2, limiting the range of high q^2 values that can be extracted accurately.

In this work we calculate the isovector nucleon form factors as a function of the momentum transfer in lattice QCD both in the quenched approximation and with two dynamical Wilson fermions. A recent study of the nucleon form factors was carried out in the quenched theory using improved Wilson fermions [5]. The current work builds on the ingredients of the previous lattice calculation and obtains results with higher accuracy at lower momentum transfers and pion masses. This enables us to determine the momentum dependence of the form factors accurately enough to have a meaningful comparison with experiment. A number of phenomenologically interesting quantities such as the r.m.s radii and dipole masses are extracted. Furthermore, we improve the accuracy of the results by constructing an optimal source for the nucleon allowing the maximum number of lattice momentum vectors to contribute. The two form factors are then extracted using an overconstrained analysis that includes all possible lattice measurements for a given value of q^2. For the quenched calculation we use a lattice of size $32^3 \times 64$ at $\beta = 6.0$, which corresponds to a lattice spacing $a \sim 0.09$ fm, obtained either by using the nucleon mass at the chiral limit or the Sommer scale. In order to assess quenching effects, we also evaluate these form factors in the unquenched theory using dynamical Wilson configurations simulated for quark masses that give pions of mass 690 MeV and 509 MeV on a lattice of size $24^3 \times 40$ [6] and 380 MeV on a lattice of size $24^3 \times 32$ [7] at $\beta = 5.6$. The lattice spacing is about 0.08 fm determined from the nucleon mass at the chiral limit. This value is consistent with the value extracted using the Sommer scale over the range of quark masses used in this work.

In lattice QCD, elastic matrix elements involving one-photon exchange require the evaluation of three-point functions. The standard procedure to evaluate three-point functions like the one we need here, namely, $G^{Nj^\mu N}(t_2, t_1; \mathbf{p}', \mathbf{p}; \Gamma)$, is to compute the sequential propagator. This can be done in two ways: In an early pioneering work, where matrix elements of a number of different hadronic states were evaluated [8], the method of choice was to couple the photon to a quark at a fixed time t_1 carrying a fixed momentum $\mathbf{q}$. Within this scheme the form factors can only be evaluated at one value of the momentum transfer. Since the current must have a fixed direction

and a fixed momentum, this approach is referred to as the fixed current approach. This method allows one to use any initial and final state without requiring further inversions, which are the time consuming part of the evaluation of three-point functions. In the second approach, which is the method used in recent studies [5,9,10], one requires that the initial state, created at time zero, and the final state, annihilated at a later fixed time t_2, have the nucleon quantum numbers. The current can couple to any intermediate time slice t_1 carrying any possible value of the lattice momentum and having any direction. Therefore, within this scheme, with a single sequential propagator one is able to evaluate all possible momentum transfers and current orientations. Since the quantum numbers of the final state are fixed, we refer to the second method as the fixed sink method. Clearly the fixed sink method is superior if our goal is the accurate determination of the momentum dependence of the nucleon form factors.

II. LATTICE TECHNIQUES

The nucleon electromagnetic matrix element for real or virtual photons can be written in the form

$$\langle N(p', s')|j_\mu|N(p, s)\rangle = \left(\frac{M_N^2}{E_N(\mathbf{p}')E_N(\mathbf{p})}\right)^{1/2} \times \bar{u}(p', s')\mathcal{O}_\mu u(p, s), \quad (1)$$

where $p(s)$ and $p'(s')$ denote initial and final momenta (spins) and E_N (M_N) is the energy (mass) of the nucleon. The operator $\mathcal{O}^\mu$ can be decomposed in terms of the Dirac form factors as

$$\mathcal{O}_\mu = \gamma_\mu F_1(q^2) + \frac{i\sigma_{\mu\nu}q^\nu}{2M_N}F_2(q^2), \quad (2)$$

where $F_1(0) = 1$ for the proton since we have a conserved current and $F_2(0)$ measures the anomalous magnetic moment. They are connected to the electric, G_E, and magnetic, G_M, Sachs form factors by the relations

$$G_E(q^2) = F_1(q^2) + \frac{q^2}{(2M_N)^2}F_2(q^2), \qquad G_M(q^2) = F_1(q^2) + F_2(q^2). \quad (3)$$

To extract the nucleon matrix element from lattice measurements, we calculate, besides the three-point function $G^{Nj^\mu N}(t_2, t_1; \mathbf{p}', \mathbf{p}; \Gamma)$, the nucleon two-point function, $G^{NN}(t, \mathbf{p})$, and look for a plateau in the large Euclidean time behavior of the ratio

$$R(t_2, t_1; \mathbf{p}', \mathbf{p}; \Gamma; \mu) = \frac{\langle G^{Nj^\mu N}(t_2, t_1; \mathbf{p}', \mathbf{p}; \Gamma)\rangle}{\langle G^{NN}(t_2, \mathbf{p}'; \Gamma_4)\rangle}\left[\frac{\langle G^{NN}(t_2 - t_1, \mathbf{p}; \Gamma_4)\rangle\langle G^{NN}(t_1, \mathbf{p}'; \Gamma_4)\rangle\langle G^{NN}(t_2, \mathbf{p}'; \Gamma_4)\rangle}{\langle G^{NN}(t_2 - t_1, \mathbf{p}'; \Gamma_4)\rangle\langle G^{NN}(t_1, \mathbf{p}; \Gamma_4)\rangle\langle G^{NN}(t_2, \mathbf{p}; \Gamma_4)\rangle}\right]^{1/2} \overset{t_2-t_1\gg 1, t_1\gg 1}{\longrightarrow} \Pi(\mathbf{p}', \mathbf{p}; \Gamma; \mu). \quad (4)$$

We use the lattice conserved electromagnetic current, $j^\mu(x)$, symmetrized on site x by taking

$$j^\mu(x) \to [j^\mu(x) + j^\mu(x - \hat{\mu})]/2 \quad (5)$$

and projection matrices for the Dirac indices

$$\Gamma_i = \frac{1}{2}\begin{pmatrix}\sigma_i & 0\\ 0 & 0\end{pmatrix}, \qquad \Gamma_4 = \frac{1}{2}\begin{pmatrix}I & 0\\ 0 & 0\end{pmatrix}, \qquad i = 1, \ldots, 3. \quad (6)$$

Throughout this work we use kinematics where the final nucleon state is produced at rest and therefore $\mathbf{q} = \mathbf{p}' - \mathbf{p} = -\mathbf{p}$. Since we aim at obtaining the full q^2 dependence of the form factors, we evaluate the three-point functions with sequential inversions through the sink. We fix $t_2 = 11(12)$ in lattice units for the quenched (unquenched) Wilson lattices and search for a plateau of $R(t_2, t_1; \mathbf{p}', \mathbf{p}; \Gamma; \mu)$ as a function of t_1. $Q^2 = -q^2$ denotes the Euclidean momentum transfer squared.

We can extract the two Sachs form factors from the ratio of Eq. (4) by choosing appropriate combinations of the direction μ of the electromagnetic current and projection matrices Γ. Provided the Euclidean times t_1 and $t_2 - t_1$ are large enough to filter the nucleon ground state, the ratio becomes time independent. Inclusion of hadronic states in the two- and three-point functions leads to the expressions written in Euclidean space

$$\Pi(\mathbf{0}, -\mathbf{q}; \Gamma_k; \mu = i) = C\frac{1}{2M_N}\epsilon_{ijk}q_j G_M(Q^2), \quad (7)$$

$$\Pi(\mathbf{0}, -\mathbf{q}; \Gamma_4; \mu = i) = C\frac{q_i}{2M_N}G_E(Q^2), \quad (8)$$

$$\Pi(\mathbf{0}, -\mathbf{q}; \Gamma_4; \mu = 4) = C\frac{E_N + M_N}{2M_N}G_E(Q^2), \quad (9)$$

where $C = \sqrt{\frac{2M_N^2}{E_N(E_N+M_N)}}$ is a factor due to the normalization of the lattice states. The first observation regarding these expressions is that the polarized matrix element given in Eq. (7), from which the magnetic form factor is determined, does not contribute for all momenta $\mathbf{q}$. In the lattice study of the $\gamma N \to \Delta$ transition [10,11], we dealt with a

similar situation where the naive Δ source was not optimal in the sense that, with one sequential propagator, not all lattice momentum vectors resulting in the same value of Q^2 contributed and an optimal source for the Δ was needed. Similarly, here one can construct an optimal linear combination for the nucleon sink that leads to

$$\begin{aligned} S_m(\mathbf{q}; i) &= \sum_{k=1}^{3} \Pi(-\mathbf{q}; \Gamma_k; \mu = i) \\ &= \frac{C}{2M_N}\{(p_2 - p_3)\delta_{1,i} + (p_3 - p_1)\delta_{2,i} \\ &\quad + (p_1 - p_2)\delta_{3,i}\}G_M(Q^2) \end{aligned} \tag{10}$$

and provides the maximal set of lattice measurements from which G_M can be extracted requiring one sequential inversion. No such improvement is necessary for the unpolarized matrix elements given in Eqs. (8) and (9), which yield G_E with an additional sequential inversion.

Unlike the $\gamma N \rightarrow \Delta$ transition, the $\gamma N \rightarrow N$ transition contains isoscalar photon contributions. This means that disconnected loop diagrams also contribute. These are generally difficult to evaluate accurately since the all-to-all quark propagator is required. In order to avoid disconnected diagrams, we calculate the isovector form factors. Assuming $SU(2)$ isospin symmetry, it follows that

$$\begin{aligned} &\left\langle p \left| \left(\frac{2}{3}\bar{u}\gamma^\mu u - \frac{1}{3}\bar{d}\gamma^\mu d\right) \right| p \right\rangle \\ &- \left\langle n \left| \left(\frac{2}{3}\bar{u}\gamma^\mu u - \frac{1}{3}\bar{d}\gamma^\mu d\right) \right| n \right\rangle = \langle p|(\bar{u}\gamma^\mu u - \bar{d}\gamma^\mu d)|p\rangle. \end{aligned} \tag{11}$$

One can therefore calculate directly the three-point function related to the right hand side of the above relation which provides the *isovector* nucleon form factors

$$\begin{aligned} G_E(q^2) &= G_E^p(q^2) - G_E^n(q^2), \\ G_M(q^2) &= G_M^p(q^2) - G_M^n(q^2). \end{aligned} \tag{12}$$

The isovector electric form factor, G_E, can therefore be obtained from the connected diagram considering either the spatial components of the electromagnetic current as given in Eq. (8) or the temporal component given in Eq. (9), while Eq. (10) is used for the extraction of the isovector magnetic form factor, G_M.

Besides using an optimal nucleon source, the other important ingredient in the extraction of the form factors is to take into account simultaneously in our analysis all the lattice momentum vectors that contribute to a given Q^2. This is done by solving the overcomplete set of equations

$$P(\mathbf{q}; \mu) = D(\mathbf{q}; \mu) \cdot F(Q^2) \tag{13}$$

where $P(\mathbf{q}; \mu)$ are the lattice measurements of the ratio given in Eq. (4) having statistical errors w_k and using the different sink types,

$$F = \begin{pmatrix} G_E \\ G_M \end{pmatrix}$$

and D is an $M \times 2$ matrix which depends on kinematical factors with M being the number of current directions and momentum vectors contributing to a given Q^2. We extract the form factors by minimizing

$$\chi^2 = \sum_{k=1}^{N}\left(\frac{\sum_{j=1}^{2} D_{kj}F_j - P_k}{w_k}\right)^2 \tag{14}$$

using the singular value decomposition of D. Given the fact that one can have a few hundred lattice momentum vectors contributing in the evaluation of the form factors, the statistical precision is highly improved. Phenomenologically interesting quantities like the r.m.s. radii and magnetic moments can thus be obtained with increased precision. There is an additional advantage by including momentum transfers $\mathbf{q}$ as well as $-\mathbf{q}$ in our analysis. The lattice conserved current given in Eq. (5) differs from the local electromagnetic current $\bar{\psi}(x)\gamma_\mu\psi(x)$ by terms of $\mathcal{O}(a)$. However when we average over $\mathbf{q}$ and $-\mathbf{q}$ these $\mathcal{O}(a)$ terms vanish.

Smearing techniques are routinely used for achieving ground state dominance before the signal from the time correlators is lost in the noisy large time limit. We use gauge invariant Wuppertal smearing, $d(x, t) \rightarrow d^{\text{smear}}(x, t)$, at the source and the sink. We smear the fermion interpolating fields according to [12]

$$d^{\text{smear}}(\mathbf{x}, t) = \sum_{\mathbf{z}} F(\mathbf{x}, \mathbf{z}; U(t))d(\mathbf{z}, t) \tag{15}$$

with the gauge invariant smearing function constructed using the hopping matrix H:

$$F(\mathbf{x}, \mathbf{z}; U(t)) = (1 + \alpha H)^n(\mathbf{x}, \mathbf{z}; U(t)), \tag{16}$$

where

$$H(\mathbf{x}, \mathbf{z}; U(t)) = \sum_{i=1}^{3}(U_i(\mathbf{x}, t)\delta_{\mathbf{x},\mathbf{y}-i} + U_i^\dagger(\mathbf{x} - i, t)\delta_{\mathbf{x},\mathbf{y}+i}). \tag{17}$$

It is well known that smearing introduces gauge noise increasing the errors on the extracted effective masses, in particular, when Wuppertal smearing is applied to both source and sink. An efficient way to reduce the ultraviolet fluctuations is to smooth out the gauge fields at the time slice of the source and the sink. One can apply various smoothing techniques such as APE [13], stout [14] or hypercubic [15] smearing on the gauge fields that are used in the hopping matrix. We found that both APE and hypercubic smearing reduce the noise and at the same time improve further the ground state overlap. In Figs. 1 and 2 we show the effective mass for the rho meson and the nucleon, respectively, using a lattice of size $16^3 \times 32$ with dirichlet boundary conditions in the temporal direc-

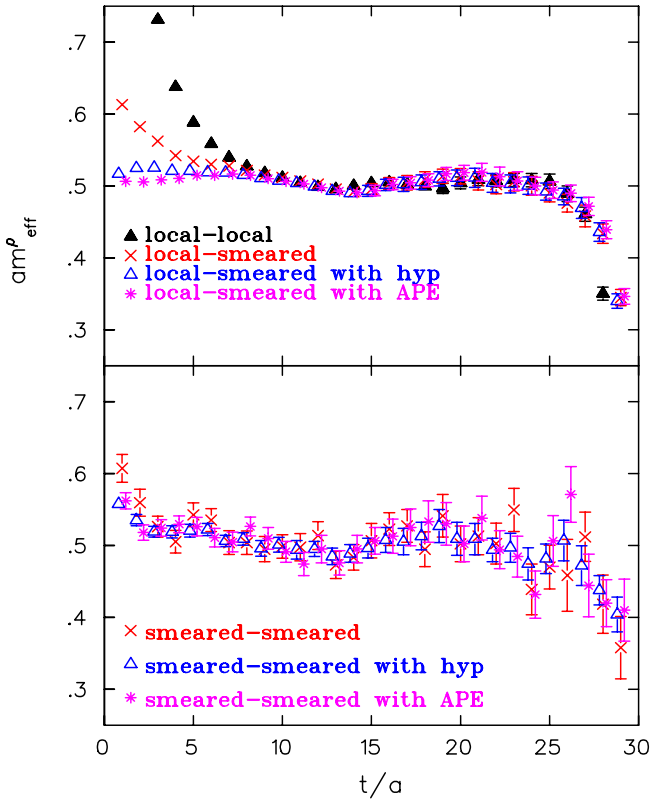

FIG. 1 (color online). The rho effective mass as a function of the time separation on a $16^3 \times 32$ quenched lattice at $\beta = 6.0$ and $\kappa = 0.153$ using Dirichlet boundary conditions in the temporal direction. In the upper graph, filled triangles show results obtained with local source and sink, crosses with Wuppertal smeared source and local sink and open triangles (asterisks) with Wuppertal smeared source using hypercubic (APE) smearing for the gauge links used in the construction of the hopping matrix $H(\mathbf{x}, \mathbf{z}; U(t))$ and local sink. The lower graph shows with crosses results obtained using Wuppertal smeared source and sink and with open triangles (asterisks) results with Wuppertal smeared source and sink where hypercubic (APE) smearing is applied to the spatial links entering the hopping matrix.

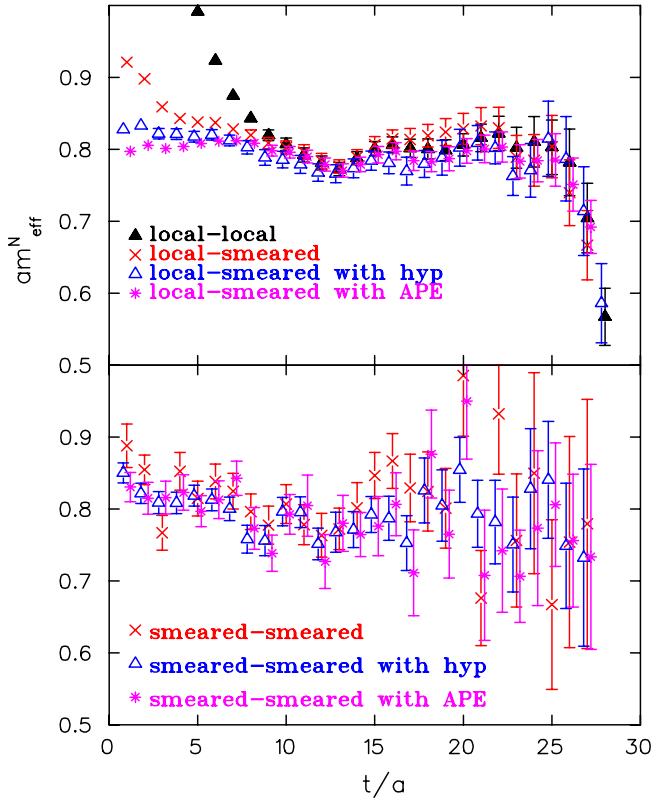

FIG. 2 (color online). The nucleon effective mass as a function of the time separation on a $16^3 \times 32$ quenched lattice at $\beta = 6.0$ and $\kappa = 0.153$. The notation is the same as that of Fig. 1.

tion to utilize the full time extent of the lattice. When only the source is smeared, both APE and hypercubic smearing improve the ground state overlap to such an extent that the plateau value is reached within a time separation as short as two time slices. When we apply Wuppertal smearing both to the source and sink, we see a reduction in the gauge noise, in particular, when hypercubic smearing is used. There is little effect on improving ground state dominance since Wuppertal smearing on both source and sink very effectively cuts down excited state contributions already after a time separation of a couple of time slices. Given the better noise reduction observed when we use hypercubic smearing we choose to apply this smearing to the links that enter the hopping matrix H. For the parameters that enter the hypercubic smearing we use the same ones as those of Ref. [15]. The parameters for the Wuppertal smearing are then optimized so that ground state dominance for the nucleon is optimal. that the parameters $\alpha = 4$ and $n = 50$ produce optimal results. These values are the same as those obtained without applying hypercubic smearing. Whereas Wuppertal smearing is applied to the source and the sink in all our computations to ensure ground state dominance at the time slice of the insertion of the electromagnetic current, hypercubic smearing is only done in the case of the unquenched configurations. This is because self averaging is less effective on smaller lattices causing the gauge noise to be more severe in the unquenched case where the simulations were done on a smaller lattice.

III. DISCUSSION OF EXPERIMENTAL RESULTS

As explained in Sec. II, we only compute the isovector part of the form factors given in Eq. (12). Therefore, to compare with experiment, it is necessary to extract from the experimentally available proton and neutron data the isovector contribution. In order to do this we need to interpolate the proton and neutron data to the same Q^2 values.

In Fig. 3 we show the proton and neutron data for the electric form factor [16,17]. As can be seen, we need to extrapolate the neutron electric form factor G_E^n at low momentum transfers and the proton electric form factor

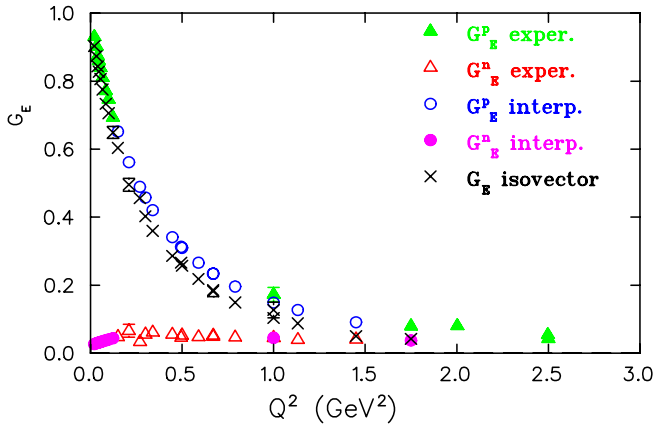

FIG. 3 (color online). The isovector electric form factor, G_E, extracted by interpolation from the measured proton and neutron electric form factors.

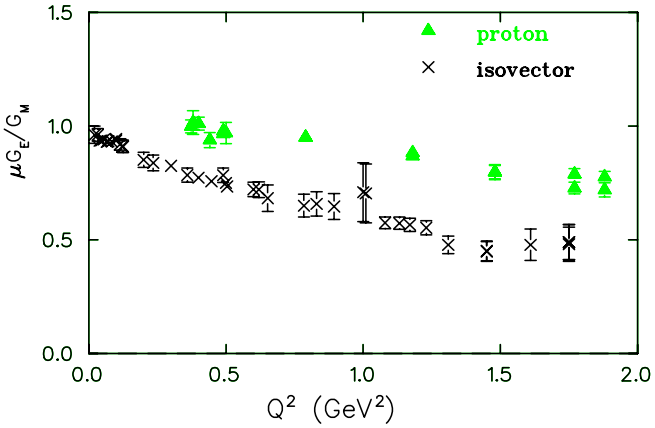

FIG. 5 (color online). The ratio of isovector form factors G_E over G_M as compared to the corresponding ratio of proton form factors from recent polarization experiments [1].

G_E^p at intermediate Q^2 values in the range $0.25 < Q^2 < 1.0$ GeV. In order to interpolate the neutron data we consider the Galster parametrization [18]

$$G_E^N(Q^2) = \frac{-\mu_n \tau}{1 + 5.6\tau} G_d(Q^2), \tag{18}$$

where $\tau = Q^2/4M_N^2$, $G_d(Q^2) = 1/(1 + Q^2/0.71)^2$ and $\mu_n = -1.91315$, which provides a good description of the data. We calculate the derivative needed for the interpolation between measured data using the Galster parametrization. Similarly, in order to interpolate the proton data, we fit to a dipole form and then use the fitted form to compute the derivative needed for the interpolation. Having G_E^n and G_E^p at the same value of Q^2, we then find the isovector contribution via Eq. (12) and plot the resulting isovector G_E in Fig. 3. As expected, the difference between G_E^p and the isovector part is small due to the smallness of G_E^n. A similar analysis is done for the magnetic form factor using the data of Ref. [16,17]. The derivative needed for the interpolation is computed either from the best dipole fit function to the available data or, in the cases where we have two measurements close to the value of Q^2 that we are interested in, by using a finite difference approximation to the derivative. The resulting isovector magnetic form factor is shown in Fig. 4. In Fig. 5 we compare the extracted isovector ratio $\mu G_E/G_M$ to recent measurements of the proton ratio $\mu_p G_E^p/G_M^p$ that showed an unexpected Q^2 dependence [1,19]. The isovector ratio for $Q^2 < 1$ GeV^2 decreases faster with Q^2 than $\mu_p G_E^p/G_M^p$, whereas for $Q^2 > 1$ GeV^2 it remains approximately constant. One of the goals is to compare this behavior with lattice calculations.

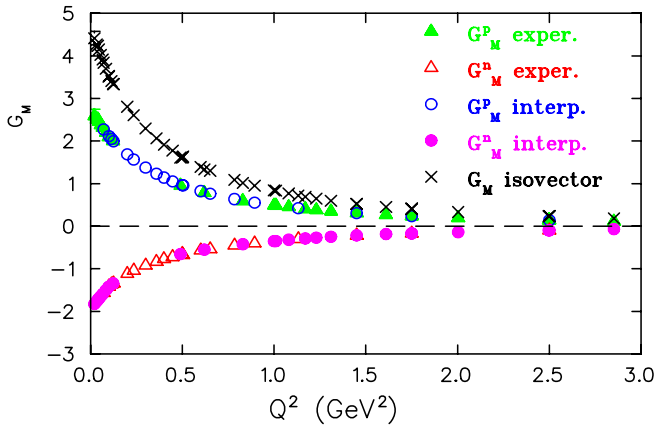

FIG. 4 (color online). The isovector magnetic form factor, G_M, extracted by interpolation from the measured proton and neutron magnetic form factors.

IV. LATTICE RESULTS

As pointed out in the Introduction, the purpose of this work is to obtain accurate results over a large range of momentum transfers. For this reason the quenched calculation is done on a lattice of size $32^3 \times 64$ enabling us to reach momentum transfers as low as about 0.15 GeV^2. The highest momentum transfer that is accessible at $\beta = 6.0$ is $2\pi/a \sim 13$ GeV. However statistical errors do not allow us to reach this maximum value. For the unquenched calculation we use configurations generated by the SESAM Collaboration [6] on a lattice of size $24^3 \times 40$ and the DESY-Zeuthen group [7] on a lattice of size $24^3 \times 32$ at $\beta = 5.6$. At this value of β the lattice spacing is close enough to the lattice spacing of the quenched lattice so that finite a-effects are comparable. Differences between the two evaluations can then be attributed to unquenching effects. In Table I we give the parameters of our calculation.

The lattice spacing is determined from the mass of the nucleon in the chiral limit. We use two different *Ansätze* for extrapolating to the chiral limit: one is $aM_N = aM_N(0) + c_0 m_\pi^2$ and the other $aM_N = aM_N(0) + c_1 m_\pi^2 + c_2 m_\pi^3$. This provides an estimate for the systematic error in

TABLE I. In the first column we give the number of configurations and in the second column the value of the hopping parameter, κ, that fixes the bare quark mass. In the third and fourth columns we give the pion and nucleon mass in lattice units. The values of the lattice spacing a are determined from the mass of the nucleon at the chiral limit. The unquenched configurations at $\kappa = 0.1575$ and $\kappa = 0.1580$ are provided by the SESAM Collaboration [6] and at $\kappa = 0.15825$ by the DESY-Zeuthen group [7].

Number of confs.	κ	am_π	aM_N
	Quenched $32^3 \times 64$ $a^{-1} = 2.14(6)$ GeV		
200	0.1554	0.263(2)	0.592(5)
200	0.1558	0.229(2)	0.556(6)
200	0.1562	0.192(2)	0.518(6)
	$\kappa_c = 0.1571$	0.	0.439(4)
	Unquenched $24^3 \times 40$ $a^{-1} = 2.56(10)$ GeV		
185	0.1575	0.270(3)	0.580(7)
157	0.1580	0.199(3)	0.500(10)
	Unquenched $24^3 \times 32$ $a^{-1} = 2.56(10)$ GeV		
200	0.15825	0.150(3)	0.423(7)
	$\kappa_c = 0.1585$	0.	0.366(13)

the extrapolated value of the nucleon mass which dominates the overall error quoted in Table I for the lattice spacing. We would like to point out that using the Sommer scale to set the scale and taking $r_0 = 0.5$ fm, values that are consistent with the ones extracted from the nucleon mass. For the quenched lattice using for r_0/a the values given in Ref. [20], we obtain $a^{-1} = 2.15$ GeV ($a = 0.093$ fm). For the unquenched lattice, the same definition gives at $\kappa = 0.1575$, $\kappa = 0.1580$, and $\kappa = 0.15825$ $a^{-1} = 2.42(4)$ GeV, $a^{-1} = 2.47(3)$ GeV, and $a^{-1} = 2.56(6)$ GeV [7] respectively. These values are consistent with the value of $a^{-1} = 2.56(10)$ GeV extracted from the nucleon mass at the chiral limit. The choice of the lattice spacing affects the physical value of Q^2 but not the values of G_E and G_M since they are computed in dimensionless units. In other words, a change in the lattice spacing a stretches the curves for G_E and G_M along the Q^2 axis and thus changes the slope.

All the quenched results for the form factors are obtained using 200 configurations and three values of the hopping parameter κ. The values of κ chosen are 0.1554, 0.1558 and 0.1562 and give a ratio of pion to rho mass $m_\pi/m_\rho = 0.64$, 0.59, and 0.50, respectively. We compare to unquenched results simulated using two flavors of Wilson fermions at $\kappa = 0.1575$, $\kappa = 0.1580$ [6] and $\kappa = 0.15825$ [7] that give a ratio of pion to rho mass of 0.69, 0.56 and 0.45, respectively. The nucleon isovector elastic form factors are extracted by solving the overconstrained set of equations defined in Eq. (13).

In Fig. 6 we compare results for the nucleon form factors obtained in the quenched theory at $\kappa = 0.1554$ using the local current and the lattice conserved current. The renormalization constant of the local current is determined by

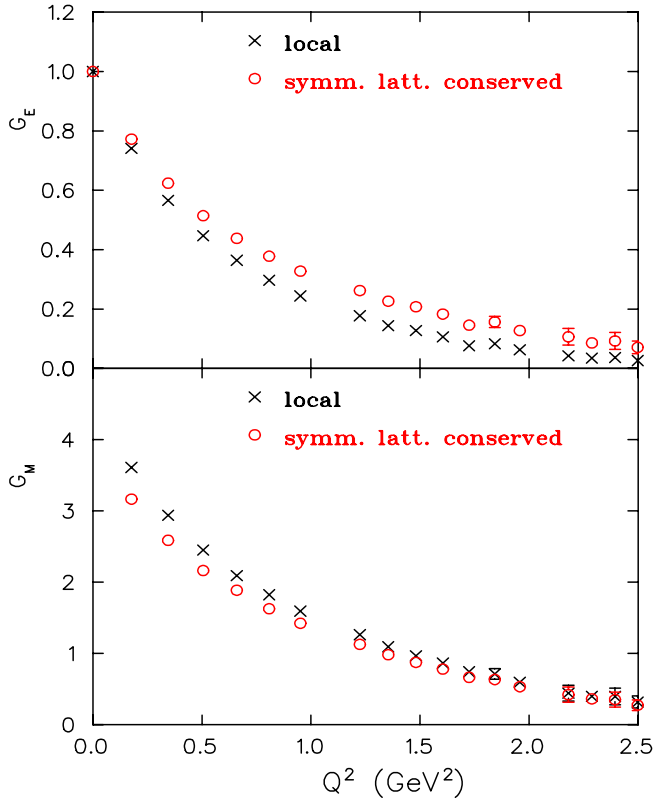

FIG. 6 (color online). G_E and G_M as functions of Q^2 in the quenched theory at $\kappa = 0.1554$ extracted using the local current $\bar{\psi}(x)\gamma_\mu\psi(x)$ (open circles) and the symmetrized lattice conserved electromagnetic current (crosses).

requiring charge conservation. The value of the renormalization constant that is $G_E^{-1}(0) = Z_v = 0.67$. As we already pointed out, averaging over all directions of $\mathbf{q}$, eliminates order a-terms in the lattice conserved current that arise from using fermionic fields at neighboring sites and the link variable that joins them. Despite the elimination of order a-terms, Fig. 6 shows a discrepancy between results obtained using the local current and the lattice conserved current. In the case of the electric form factor, the results from the local current have smaller values, whereas for the magnetic case they have higher values. This means that these differences will be amplified in the ratio of the two form factors. Since in our approach the order a-terms are eliminated in the conserved current, there is no other obvious improvement, as far as the current is considered, that we can implement. Given that the lattice current is the one that ensures charge conservation, the consistent approach is to use this current. A further argument for this choice is provided by considering the electric form factor G_E, which can be evaluated using Eq. (8) or Eq. (9). In Fig. 7 we compare the electric form factor extracted using Eq. (9) with that extracted from Eq. (8). As can be seen for Q^2 larger than about 0.5 GeV^2 there is perfect agreement when using the lattice conserved current. The disagreement at lower Q^2 can be understood from

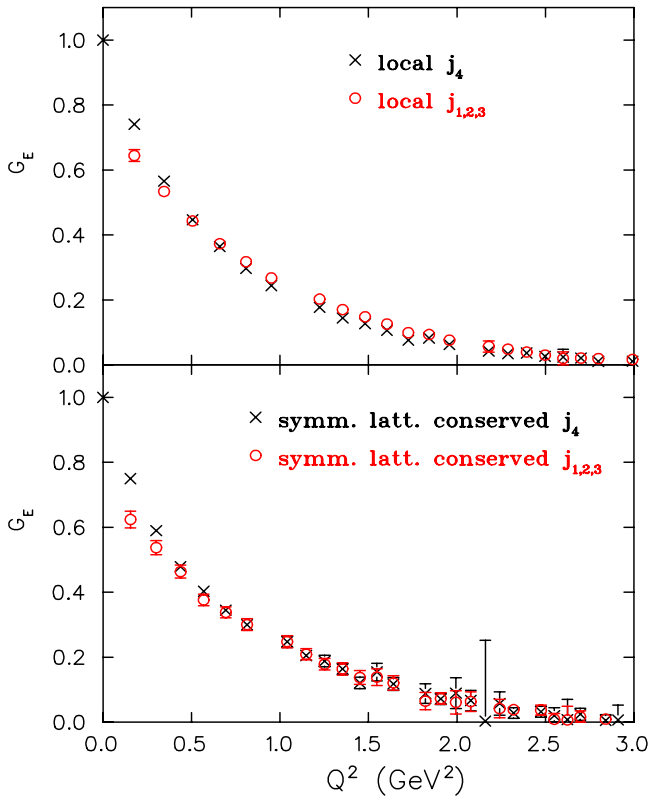

FIG. 7 (color online). G_E as a function of Q^2 in the quenched theory at $\kappa = 0.1554$ extracted using Eq. (8) (open circles) when the electromagnetic current is in the spatial direction and using Eq. (9) (crosses) with the electromagnetic current in the temporal direction. The top graph show results extracted using the local current $\bar{\psi}(x)\gamma_\mu\psi(x)$ and the lower using the symmetrised lattice conserved current.

the dependence on the momentum transfer appearing in the right hand side of Eq. (8). As $\mathbf{q} \to \mathbf{0}$ the right hand side of Eq. (8) tends to zero. Inverting to obtain G_E from the measured $\Pi(\mathbf{0}, -\mathbf{q}; \Gamma_4; \mu = i)$ becomes inaccurate resulting in an erroneous value for G_E. Using the local current on the other hand, we observed small differences between the results obtained using Eq. (8) and (9) up to values of Q^2 as large as 2 GeV^2, which indicates a lattice artifact. Therefore, given charge conservation and consistency of the results coming from two different determinations of G_E, we conclude that the lattice conserved current is the best choice for the evaluation of the form factors within our current framework. Furthermore for $Q^2 < 0.5$ GeV^2, we will only use Eq. (9) for the determination of G_E whereas for higher Q^2 values both Eqs. (8) and (9) will be used.

In Fig. 8 we show the results for the electric form factor at three values of κ for the quenched and the unquenched cases. On the scale of this figure, only a weak quark mass dependence is seen. Both quenched and unquenched results decrease as the quark mass decreases, yielding a larger slope at small Q^2, which is the expected behavior. In order to better resolve differences in our data, we plot in

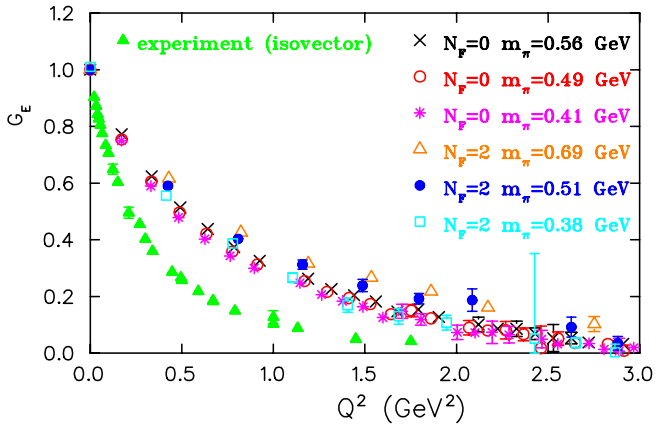

FIG. 8 (color online). The isovector electric form factor, G_E, as a function of Q^2. We show quenched lattice results at $\kappa = 0.1554$ (crosses), at $\kappa = 0.1558$ (open circles) and at $\kappa = 0.1562$ (asterisks). The unquenched results are shown at $\kappa = 0.1575$ (open triangles) $\kappa = 0.1580$ (filled circles) and at $\kappa = 0.15825$ (open squares). The filled triangles show experimental results for the isovector electric form factor extracted using the analysis described in Sec. III and data from Refs. [16,17].

Fig. 9 the ratio of the electric form factor to the proton dipole form factor, G_E/G_d. Both quenched and unquenched results are clearly higher than the experimentally determined data, decreasing with the quark mass. The unquenched results in general show a stronger quark mass dependence leading to smaller values in the chiral limit. The main observation, however, is that both quenched and unquenched results have a different Q^2 dependence as compared to the results extracted from experimental measurements: The lattice data have a positive slope at small Q^2 whereas experiment favors a negative slope. The two main uncertainties regarding the lattice results are finite a-effects and whether we are close enough to the chiral limit. Since unquenched Wilson configura-

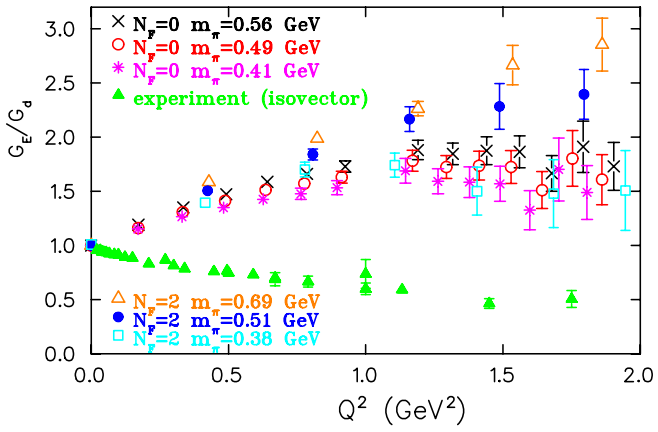

FIG. 9 (color online). The isovector electric form factor, G_E, divided by the proton dipole form factor as a function of Q^2. The notation is the same as in Fig. 8.

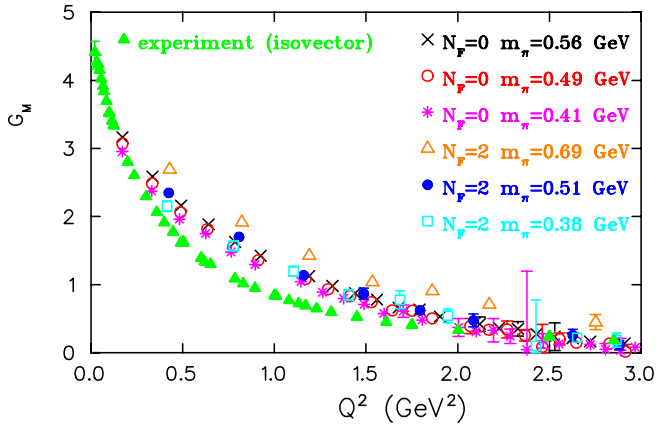

FIG. 10 (color online). The isovector magnetic form factor, G_M, as a function of Q^2. The notation is the same as in Fig. 8.

tions are only available at this lattice spacing, assessing whether finite a-effects can explain this behavior is beyond the scope of the present study. Also dynamical Wilson configurations at smaller quark masses on large enough volumes are not available so at present we cannot evaluate these form factors closer to the chiral limit.

The evaluation of the magnetic form factor G_M is done using Eq. (10), which employs the optimal source. The results for the magnetic form factor are shown in Fig. 10 and, on the scale of this figure, the lattice results are closer to experiment than the results for G_E. Again, quenched and unquenched results decrease with the quark mass with the unquenched results showing a stronger quark mass dependence. The stronger quark mass dependence of the unquenched data at low Q^2 is more clearly seen in Fig. 11 where we plot the ratio G_M/G_d. Again in the chiral limit we expected a reduction in the value of G_M bringing lattice results closer to experiment. It is worth noting that the experimentally determined isovector form factor is very well described by the dipole form $G_d(Q^2)$ whereas the lattice data clearly show deviations from the dipole form

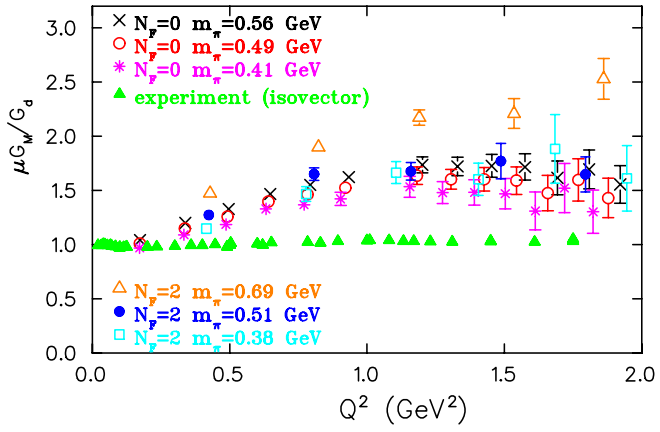

FIG. 11 (color online). The isovector magnetic form factor, G_M, divided by the proton dipole form factor taking $\mu = 4.71$ as a function of Q^2. The notation is the same as in Fig. 8.

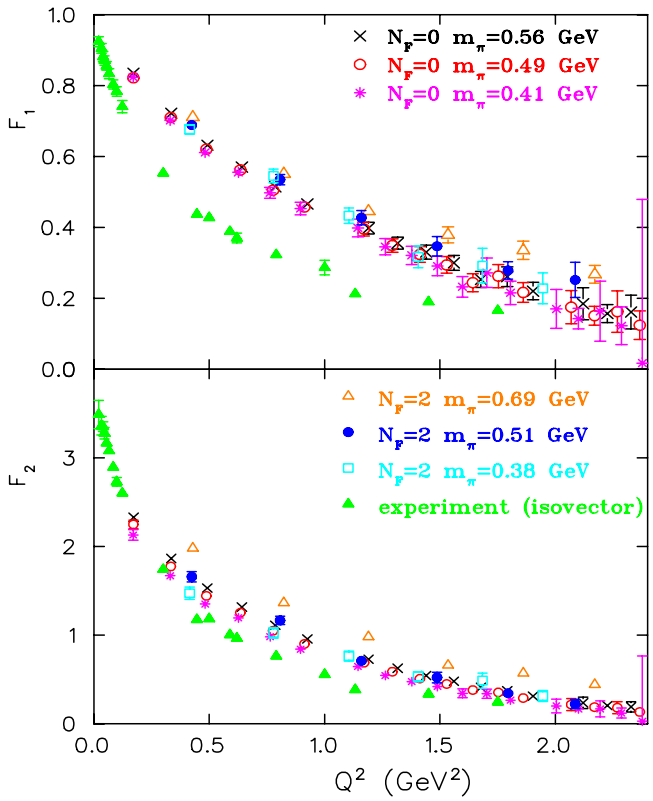

FIG. 12 (color online). The isovector form factors F_1 (top) and F_2 (bottom), as a function of Q^2. The notation is the same as in Fig. 8.

at least for the mass range considered in this work. To directly compare, however, to experiment one has to carry out a chiral extrapolation of G_E and G_M. This is discussed in the next section. Ideally one must also carry out the continuum limit using lattices of different values of a, which is however beyond the scope of the present work. For completeness, we show in Fig. 12 the form factors F_1 and F_2, which are a linear combination of G_E and G_M. What can be seen is that, in the case of F_1, the lattice

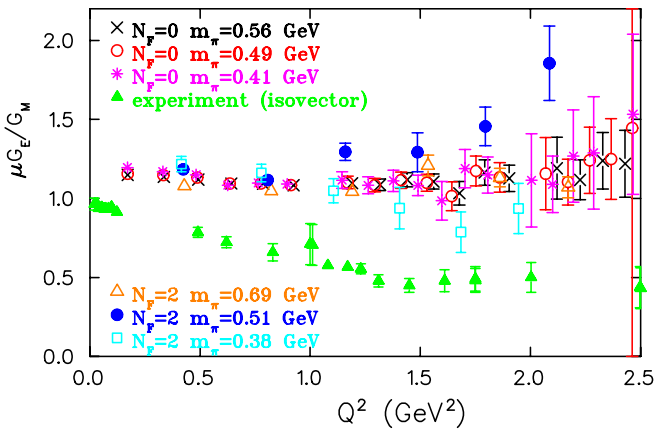

FIG. 13 (color online). The isovector ratio, $\mu G_E/G_M$, as a function of Q^2. The notation is the same as in Fig. 8.

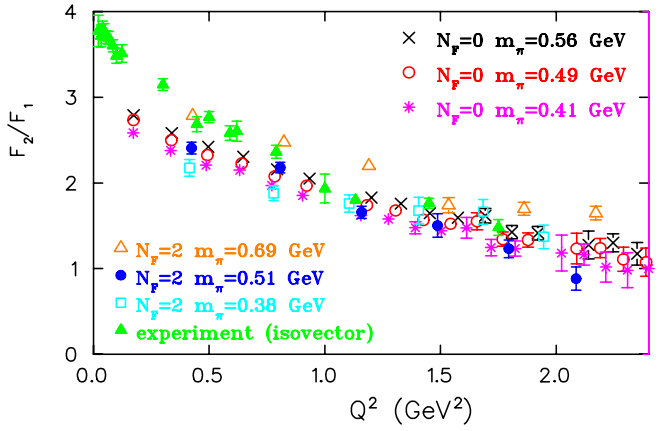

FIG. 14 (color online). The isovector ratio, F_2/F_1, as a function of Q^2. The notation is the same as in Fig. 8.

results show only a very weak increase in the slope as the quark decreases. The slope of F_1 is directly related to the transverse size of the hadron [4] and one expects an increase in the slope as the quark mass decreases, which is not observed in the lattice data. On the other hand, in the case of F_2 one observes a stronger quark mass dependence. This stronger quark mass dependence potentially can lead to agreement with experiment after the chiral extrapolation is carried out. In the case of F_1, given the weaker quark mass dependence and the larger deviation from experiment, one would require a nontrivial mass dependence at small quark masses to reconcile the lattice data with experiment. The experimentally interesting ratio of form factors, $\mu G_E/G_M$, is shown in Fig. 13. As can be seen it shows very little dependence on the quark mass and, modulo finite a-effects, it can already be compared to experiment. The ratios obtained in the quenched and the unquenched theory are in agreement with each other but disagree with the behavior extracted from experiment. This disagreement is also clearly seen in the ratio F_2/F_1 shown in Fig. 14 especially at small Q^2.

V. EXTRAPOLATION TO THE CHIRAL LIMIT

In order to compare our results for G_E and G_M with experiment, we must extrapolate the lattice results to the chiral limit. The quark masses used in this work correspond to pion masses in the range 560 to 410 MeV in the quenched theory and 690 to 380 MeV in the unquenched theory. Pion cloud effects are expected to be small in this range of pion masses and therefore we expect the results to show a linear dependence in the pion mass squared, m_π^2. To carry out correctly the chiral extrapolation of the form factors one would need chiral perturbation theory in the range of pion masses that we have results and valid for momentum transfers Q^2 up to about 2 GeV^2. The only chiral expansion for the form factors presented recently is limited to small momentum transfers [21]. On the other hand, one expects that for values of $Q^2 \gtrsim 0.5$ GeV^2 nonanalytic terms are suppressed and a linear dependence in m_π^2 provides a good description to the data. In Fig. 15 we plot the magnetic and electric form factors for the three lowest Q^2 values as a function of m_π^2. We used Eq. (9) to extract the electric form factor since $Q^2 < 0.5$ GeV^2 and only Eq. (9) yields reliable results. For these lowest values of Q^2 nonanalytic terms could be important and should be visible as the pion mass decreases. As can be seen in this figure, a linear dependence is consistent for the quenched data at the three lowest Q^2 values. The unquenched data are also consistent with a linear behavior. This is indeed what is observed also for the higher Q^2 values as can be seen in Fig. 15 where we show the unquenched results at $Q_0^2 = 1.37$ GeV^2 where by $Q_0^2 = 2M_N(E_N - M_N)$ we denote the momentum transfer squared in the chiral limit obtained by using the physical nucleon mass. It is therefore reasonable to extrapolate the form factors linearly in m_π^2 to obtain results in the chiral limit. Since Q^2 depends on the mass of the nucleon it changes with the quark mass and we

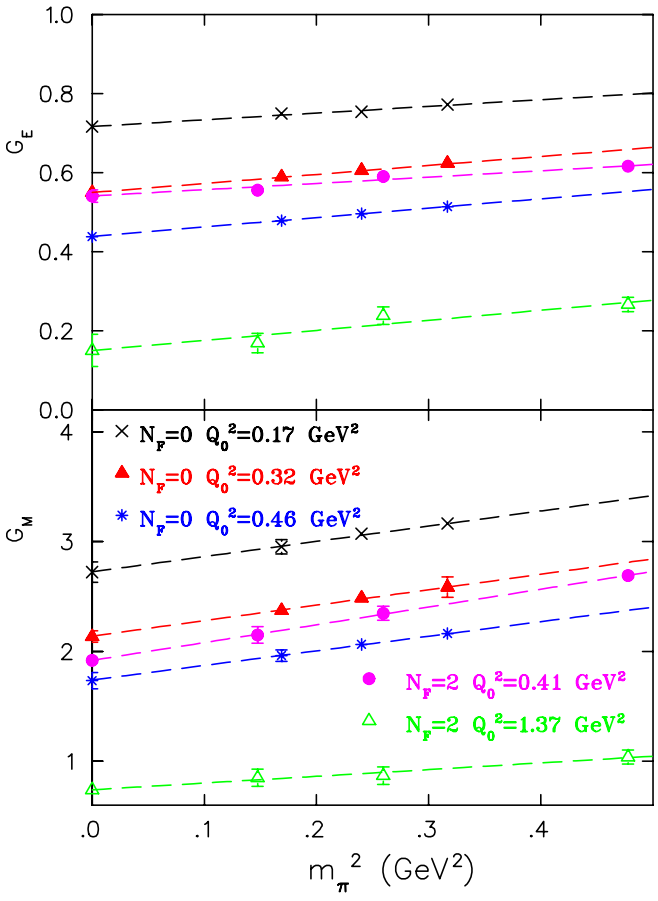

FIG. 15 (color online). The isovector electric (upper) and magnetic (lower) form factors as a function of m_π^2 for the three lowest Q^2 values available on our quenched lattice. With Q_0^2 we denote the momentum transfer square in the chiral limit. Unquenched results are shown with the filled circles at the lowest available Q^2-value and with the open triangles at $Q_0^2 = 1.37$ GeV^2.

need to extrapolate form factors evaluated at somewhat different Q^2. To leading order, Q^2 decreases linearly with m_π^2. Therefore we perform a fit to the form

$$f(Q^2, m_\pi^2) = f(Q_0^2, 0) + Am_\pi^2, \tag{19}$$

where we extract the form factor at the chiral limit at Q_0^2. As can be seen in Fig. 15 this linear behavior is well satisfied for $Q_0^2 = 1.37$ GeV^2 the largest value shown in the figure. Another option is to interpolate lattice data obtained for different quark masses at Q_0^2 and perform a chiral extrapolation at this constant value of the momentum transfer squared. Only the value A of the slope should be affected whereas $f(Q_0^2, 0)$ should not change. We checked these two procedures for various values of Q^2. We found that the results for $f(Q_0^2, 0)$ obtained using these two procedures were indeed consistent. In what follows we will therefore use Eq. (19) for the chiral extrapolation.

The resulting values at the chiral limit are shown in Fig. 16 for G_E and G_M. The disagreement with experiment is larger in the case of the electric form factor and can be traced to its weak quark mass dependence. Lattice results also show a different Q^2 dependence as compared to experiment. The linearly extrapolated lattice results are closer to experiment in the case of the magnetic form factor. For comparison, we show in Fig. 17 the lattice results for F_1 and F_2 after linearly extrapolated to the chiral limit. There is little deviation between unquenched and quenched results at the chiral limit. In addition, for $Q^2 > 0.5$ GeV^2 there is good agreement between the lattice results for F_2 and the results extracted from experiment. This is not the case for F_1 where the experimentally determined isovector F_1 decays faster as compared to the lattice results.

In order to obtain the isovector magnetic moment $G_M(0)$, one needs to evaluate the magnetic form factor G_M at $Q^2 = 0$. This requires an extrapolation of lattice results to $Q^2 = 0$. One fitting Ansatz commonly used to describe the Q^2 dependence of the form factors is a dipole. We thus consider a dipole form with different isovector magnetic and electric dipole masses squared, M_m and M_e:

$$G_M(Q^2) = \frac{G_M(0)}{(1 + \frac{Q^2}{M_m})^2}, \tag{20}$$

$$G_E(Q^2) = \frac{1}{(1 + \frac{Q^2}{M_e})^2}. \tag{21}$$

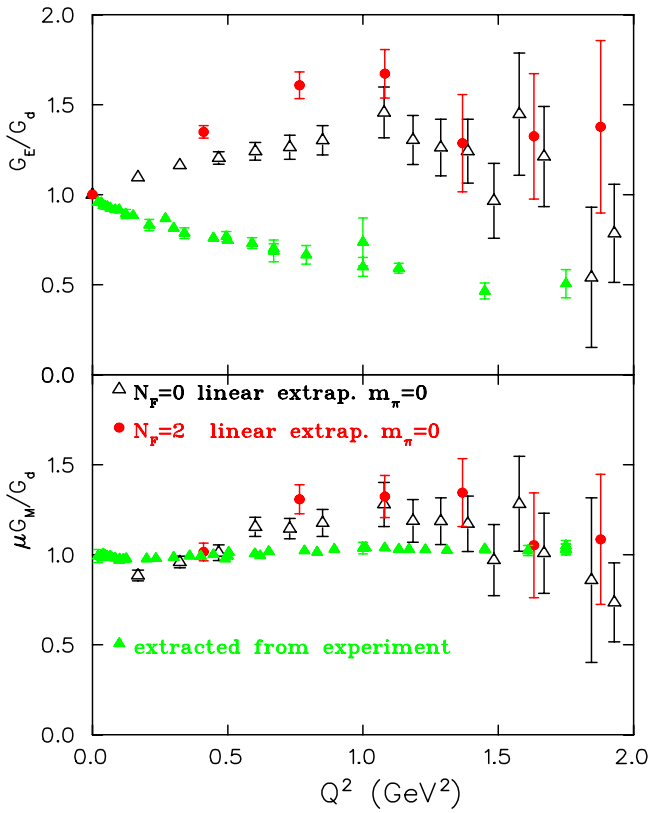

FIG. 16 (color online). The ratios G_E/G_d (upper) and $\mu G_M/G_d$ (lower) as a function of Q^2 at the chiral limit. Open triangles show quenched results obtained at the chiral limit by linear extrapolation of the form factors G_M and G_E and filled circles denote the corresponding unquenched results. The results for these isovector ratios extracted from experiment are shown by the filled triangles.

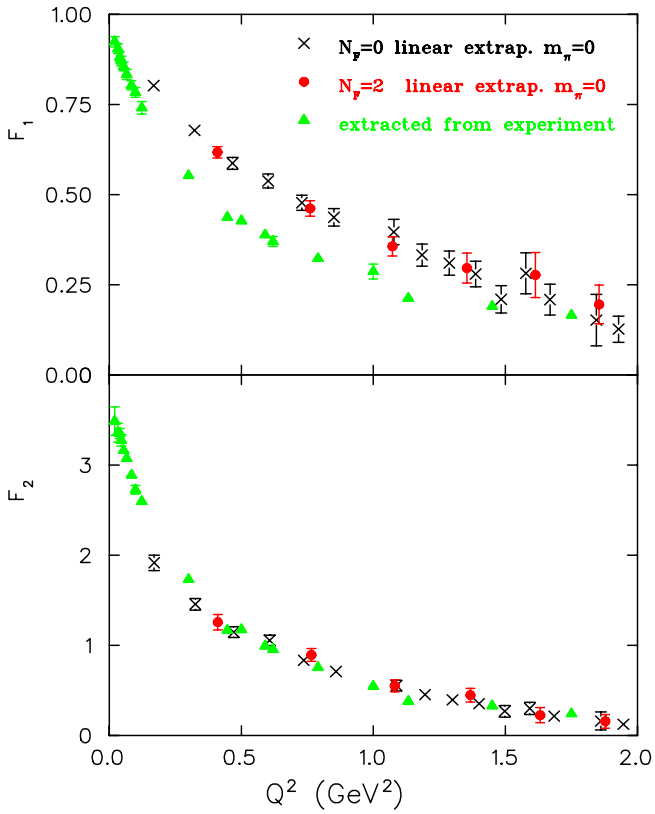

FIG. 17 (color online). The form factors F_1 (upper) and F_2 (lower) as a function of Q^2. Crosses show quenched results at the chiral limit, and filled circles unquenched results. The results extracted from experiment are shown by the filled triangles.

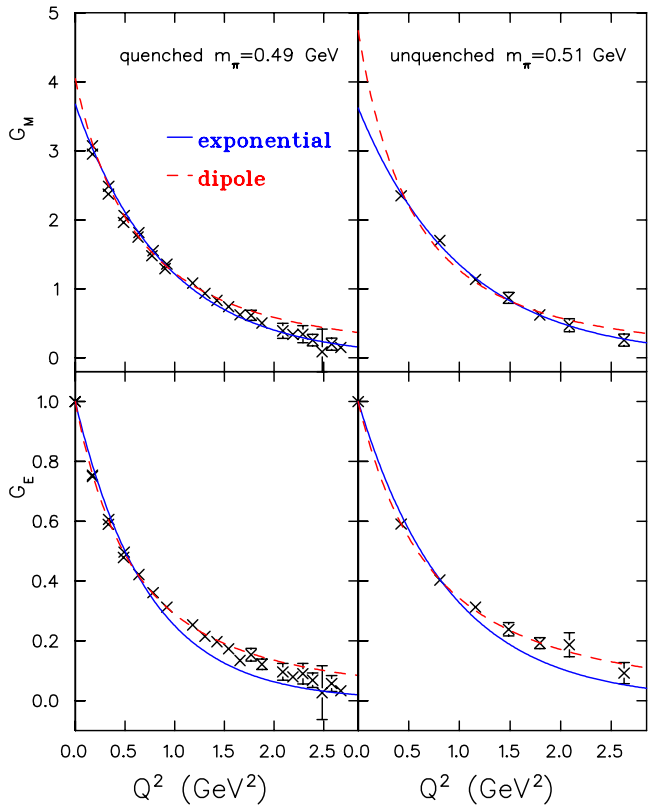

FIG. 18 (color online). The magnetic (upper) and electric (lower) form factors for the quenched and the unquenched cases with fits to dipole (dashed line) and exponential (solid line) forms.

A good fit giving χ^2/(degree of freedom) ~ 1 is obtained when the form factors are fitted for $Q^2 \lesssim 2.5$ GeV^2. The quality of the fits is shown in Fig. 18, where we show quenched and unquenched data at $\kappa = 0.1558$ and $\kappa = 0.1580$ respectively. On the same figure, we include a fit to an exponential form. For the magnetic form factors, an exponential Ansatz describes very well the Q^2 dependence, especially in the quenched case where it is in fact favored. An exponential fit, however, does not provide a good fit to the electric form factors. Therefore in order to extract the r.m.s. radii we will use throughout a dipole Ansatz. In Table II we give the magnetic moment, $G_M(0)$, and the magnetic and electric dipole masses extracted from the dipole fits to the quenched and unquenched results at each value of the quark mass. The dipole masses extracted from the fits are generally larger than the value of $M_d = 0.71$ GeV^2 entering in the proton form factor G_d. This is consistent with the fact that the lattice data normalized with G_d are not constant but increase as a function of Q^2 as shown in Figs. 9 and 11. In the same Table we also give the values extracted by applying dipole fits to the form factors after they have been linearly extrapolated to the chiral limit. Since the dipole masses decrease with the quark mass, the fits of the form factors at the chiral limit yield a smaller value for M_e and M_m. In the unquenched case these values are rather close to the value of the proton dipole mass, M_d.

The quark mass dependence of the magnetic moments extracted from the dipole fits is presented in Fig. 19. A linear extrapolation of the quenched results to the chiral limit leads to $G_M(0) = 3.67(3)$. As expected, this value is in agreement with the value obtained from the dipole fit of G_M at the chiral limit quoted in Table II. This agreement confirms that our extrapolation using Eq. (19) yields results consistent to those obtained by extrapolating to the chiral limit at constant value of Q^2. The slope of F_1 at $Q^2 = 0$ determines the transverse size of the hadron, $\langle r_1^2 \rangle = -4dF_1/dQ^2|_{Q^2=0}$. In the nonrelativistic limit the r.m.s. radius is related to the slope of the form factor at zero momentum transfer. Therefore the r.m.s. radii can be directly obtained from the values of the dipole masses by using

$$\langle r_i^2 \rangle = -\frac{6}{F_i(Q^2)} \frac{dF_i(Q^2)}{dQ^2}\bigg|_{Q^2=0} = \frac{12}{M_i}, \qquad i = 1, 2. \tag{22}$$

TABLE II.

κ	$G_M(0)$	M_m (GeV^2)	M_e (GeV^2)	$\langle r_1^2 \rangle^{1/2}$ (fm)	$\langle r_2^2 \rangle^{1/2}$ (fm)
Quenched $32^3 \times 64$ $a^{-1} = 2.14(6)$ GeV					
0.1554	4.11(7)	1.29(4)	1.24(1)	0.520(5)	0.64(1)
0.1558	4.02(8)	1.28(4)	1.15(1)	0.538(6)	0.64(1)
0.1562	3.90(9)	1.19(4)	1.08(1)	0.550(8)	0.66(1)
$\kappa_c = 0.1571$	3.73(13)	1.03(5)	0.90(2)	0.585(13)	0.72(2)
Unquenched $24^3 \times 40$ $a^{-1} = 2.56(10)$ GeV					
0.1575	4.45(14)	1.53(7)	1.55(1)	0.467(7)	0.58(2)
0.1580	4.34(43)	1.23(16)	1.41(2)	0.462(23)	0.67(5)
Unquenched $24^3 \times 32$ $a^{-1} = 2.56(10)$ GeV					
0.15825	4.10(46)	1.17(17)	1.19(4)	0.500(29)	0.68(6)
$\kappa_c = 0.1585$	3.25(48)	0.792(17)	0.66(4)	0.756(36)	0.79(13)

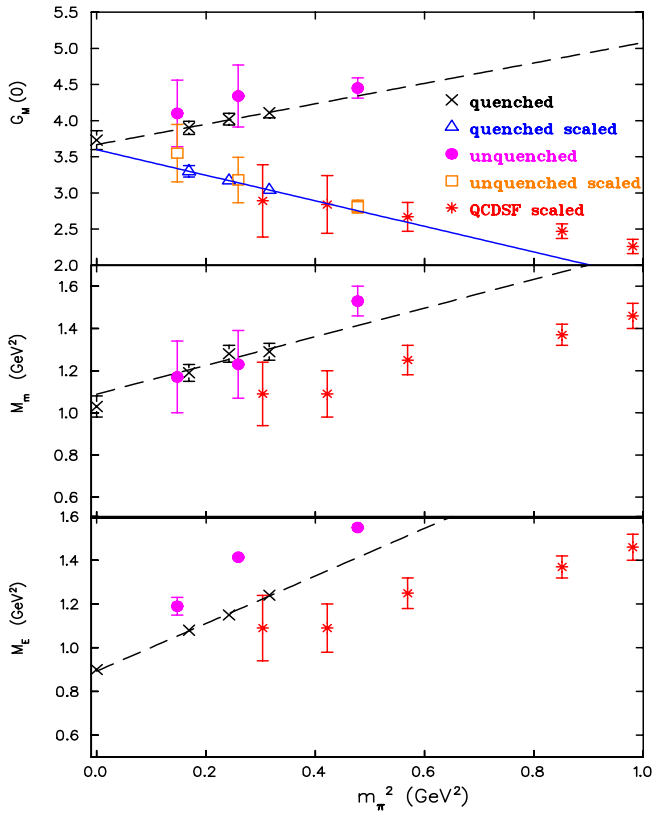

FIG. 19 (color online). The magnetic moment (upper), the magnetic (middle) and electric (lower) dipole mass extracted from fits, assuming a dipole dependence for the form factors, are shown as a function of the pion mass squared. The dashed line is a linear fit to the quenched results. The values at the chiral limit are obtained from fitting the linearly extrapolated form factors at the chiral limit to a dipole Ansatz. Our quenched data are shown by the crosses, the unquenched data by the filled circles, our scaled quenched (unquenched) magnetic moments by the open triangles (open squares) and the quenched results from Ref. [5] by the asterisks.

The electric and magnetic radii are given by $\langle r^2_{e,m}\rangle = 12/M_{e,m}$ and can be directly evaluated from the values given in Table II. We can also obtain $\langle r_i^2\rangle$ in terms of M_m and M_e using the relations

$$\langle r_1^2\rangle = \frac{12}{M_e} - \frac{3F_2(0)}{2M_N^2}, \qquad \langle r_2^2\rangle = \frac{12(1+F_2(0))}{F_2(0)M_m} - \frac{\langle r_1^2\rangle}{F_2(0)}. \tag{23}$$

In Eq. (23) we take $F_2(0) = G_M(0) - 1$ extracted from the dipole fits. Alternatively, one can fit directly the F_1 and F_2 form factors and obtain the dipole masses M_1 and M_2. What one finds via this procedure is that the values for $\langle r_i^2\rangle$ tend to be smaller than but consistent within errors with the ones extracted using Eq. (23). The quark mass dependence of the magnetic and electric dipole masses is also shown in Fig. 19. A linear dependence in m_π^2 is consistent for the quenched results yielding, at the chiral limit, $M_m = 1.09(10)$ GeV^2 and $M_e = 0.89(4)$ GeV^2. Again, these values are in agreement with the values extracted by fitting the form factors after they have been linearly extrapolated to the chiral limit as can be seen from the values quoted in Table II. After scaling the magnetic moments by the ratio of the physical nucleon mass to the one measured on the lattice, they become an increasing faction of m_π^2 as can be seen in Fig. 19. In the same figure we also include the quenched results obtained from Ref. [5], that used perturbatively improved Wilson fermions. We choose data at $\beta = 6.0$ where the value of the lattice spacing extracted from their nucleon mass is $a^{-1} = 1.83$ GeV. This is close enough to our quenched lattice to allow a meaningful comparison. It is reassuring that, despite the fact that different currents and Wilson fermions were used in the two calculations, results at a similar pion mass are consistent.

As the pion mass decreases, one expects cloud pion contributions to become important and deviations from the linear dependence on m_π^2 should be observed, in particular, at low Q^2, thus affecting the values of $G_M(0)$ and the dipole masses and hence the r.m.s. radii. In a recent calculation the quark mass dependence of the isovector magnetic moment and radii was determined. This was done within a chiral effective theory with explicit nucleon and Δ degrees of freedom [5,22]. The isovector anomalous magnetic moment as a function of the pion mass to one-loop order is given by [22]

$$\begin{aligned}\kappa_v(m_\pi) = \kappa_v(0) &- \frac{g_A^2 m_\pi M_N}{4\pi F_\pi^2} \\ &+ \frac{2c_A^2\Delta M_N}{9\pi^2F_\pi^2}\left[R_1(m_\pi) + \log\left(\frac{m_\pi}{2\Delta}\right)\right] \\ &- 8E_1 M_N m_\pi^2 + \frac{4c_A c_V g_A M_N m_\pi^2}{9\pi^2F_\pi^2}\log\left(\frac{2\Delta}{\lambda}\right) \\ &+ \frac{4c_A c_V g_A M_N m_\pi^3}{27\pi F_\pi^2\Delta} - \frac{8c_A c_V g_A \Delta^2 M_N}{27\pi^2F_\pi^2} \\ &\times\left[\left(1-\frac{m_\pi^2}{\Delta^2}\right)R_1(m_\pi) + \left(1-\frac{3m_\pi^2}{2\Delta^2}\right)\log\left(\frac{m_\pi}{2\Delta}\right)\right],\end{aligned} \tag{24}$$

where

$$R_1(m) = \frac{\sqrt{\Delta^2 - m^2 + i\epsilon}}{2\Delta}\log\left(\frac{\Delta + \sqrt{\Delta^2 - m^2 + i\epsilon}}{\Delta - \sqrt{\Delta^2 - m^2 + i\epsilon}}\right) \tag{25}$$

and $\Delta = M_\Delta - M_N$ is the Δ-nucleon mass splitting $M_\Delta - M_N$. Following Ref. [22] we fix g_A, c_A, F_π, M_N and Δ to their physical values given in Table III and vary $\kappa_v(0)$, c_V and E_1. The counter term E_1 depends on the regularization scale λ for which we take $\lambda = 0.6$ GeV in order to make contact with Ref. [22]. As can be seen in Fig. 19 the

TABLE III. The first column lists the fixed parameters and the second their values at the physical pion mass. The third column gives the fitted parameters and the fourth the values determined by fitting to Eq. (24) for the magnetic moment, to Eq. (26) for r_1^2 and to Eq. (27) for r_2^2.

Fixed parameter	Empirical value	Fitted parameter	Fitted value
g_A	1.267	$\kappa_v(0)$	6.08(11)
c_A	1.125	c_V	$-2.75(50)$ GeV^{-1}
F_π	0.0924 GeV	E_1	$-5.60(5)$ GeV^{-3}
M_N	0.9389 GeV	B_{10}	$-0.3(3)$ GeV^{-3}
Δ	0.2711 GeV	B_{c2}	0.61(4)

magnetic moments in the quenched and unquenched theory are in agreement and therefore we use both sets to fit to the chiral effective theory result given in Eq. (24). Fitting to the rescaled data we obtain the curve shown by the solid line in Fig. 20. In Table III we give the values of $\kappa_v(0)$, c_V and E_1 extracted from the fit. The dashed lines give the maximal error band determined by varying the fitted parameters by the quoted errors. The extrapolated value of the magnetic moment at the physical pion mass is in agreement with experiment.

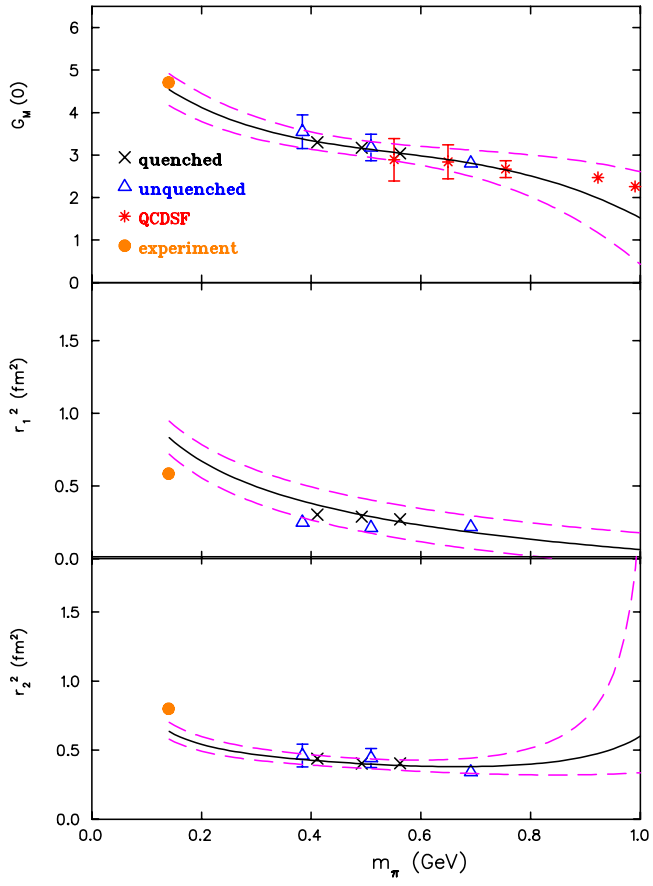

FIG. 20 (color online). Chiral extrapolation of the magnetic moment (upper) and the r.m.s radii r_1 (middle) and r_2 (lower). The solid line is the best fit to the effective chiral theory results. The dashed lines show the maximal allowed error band using the errors on the fitted parameters.

For the isovector Dirac and Pauli radii we use the one-loop results given in Ref. [5]:

$$r_1^2 = -\frac{1}{(4\pi F_\pi)^2}\left[1 + 7g_A^2 + (10g_A^2 + 2)\log\left(\frac{m_\pi}{\lambda}\right)\right] - \frac{12B_{10}}{(4\pi F_\pi)^2} + \frac{c_A^2}{54\pi^2 F_\pi^2}\left[26 + 30\log\left(\frac{m_\pi}{\lambda}\right) + 30R_2(m_\pi)\right] \tag{26}$$

and

$$r_2^2 = \frac{1}{\kappa_v(m_\pi)}\left\{\frac{g_A^2 M_N}{8F_\pi^2\pi m_\pi} + \frac{c_A^2 M_N}{9F_\pi^2\pi^2\Delta}R_2(m_\pi) + 24M_N B_{c2}\right\}, \tag{27}$$

where

$$R_2(m) = \frac{\Delta}{2\sqrt{\Delta^2 - m^2 + i\epsilon}}\log\left(\frac{\Delta + \sqrt{\Delta^2 - m^2 + i\epsilon}}{\Delta - \sqrt{\Delta^2 - m^2 + i\epsilon}}\right). \tag{28}$$

The only parameter that we vary in fitting the Dirac radius is the counter term B_{10}, which depends on the scale λ and parametrizes short distance contributions. Once the magnetic moment is fitted, the only parameter entering in the Pauli radius that we vary is the counter term B_{c2}, which is the analogue of B_{10}. The resulting fits for the radii are shown in Fig. 20. The pion mass dependence of the Dirac radius is not well reproduced. Since this is related to the slope of F_1 this is not surprising given that the lattice results have a different slope from the experimental one and hardly show any quark mass dependence.

VI. CONCLUSIONS

The elastic isovector nucleon form factors are calculated in lattice QCD with Wilson fermions both in the quenched approximation and using unquenched configurations [6,7] with two flavors of dynamical Wilson fermions. The current work presents an improvement to a previous lattice study [5], carried out in the quenched approximation, in a number of ways: In the quenched theory we use a lattice of twice the spatial and temporal size. This allows an accurate determination of the form factors at lower values of Q^2, enabling us to extract more reliably the dependence on Q^2. In addition, the quenched calculation is carried out at smaller quark masses, bringing us closer to the chiral limit. Preliminary quenched results on a lattice of size $32^3 \times 48$ at $\beta = 6.0$ using Wilson fermions were presented in Ref. [23]. Although the low Q^2 range probed is the same as in the current work, only results after linear extrapolation to the chiral limit, using data computed at two light quark masses and thus carrying large statistical errors,

were discussed. Furthermore in this work we evaluated the form factors in the unquenched theory allowing us to assess unquenching effects for pion masses down to about 380 MeV. Finally, an improved overconstrained analysis is carried out where the nucleon source is optimized and all the lattice momentum vectors contributing to a given value of Q^2 are taken into account. The resulting statistical errors are therefore small enough that a comparison between quenched and unquenched results is meaningful. What is that both quenched and unquenched results for both form factors decrease with the quark mass. Unquenching effects are small and the results obtained after a linear extrapolation in m_π^2 to the chiral limit fall on the same curve as can be seen, for example, in Fig. 17 for F_1 and F_2. Assuming lattice artifacts are under control, this improved analysis gives results that can be compared to experiment by extracting the isovector form factors from the proton and neutron measurements of these quantities. The largest uncertainties regarding our lattice results are how close to the continuum limit these results are and the chiral extrapolation. With these caveats in mind, the comparison of the results obtained here to experiment reveals interesting features: Both quenched and unquenched results are higher than the experimentally extracted form factors, with the deviations being larger in the case of the electric isovector form factor. In the quenched case, where we have very accurate results at low momentum transfer, that the electric form factor decreases slower with Q^2 compared to what is observed experimentally. This different behavior is also reflected in the ratio $\mu G_E/G_M$, where the lattice results are constant up to about $Q^2 = 2.5$ GeV^2 whereas the experimentally determined data decrease as a function of Q^2. In the range of quark masses investigated in this work, the quark mass dependence observed for $\mu G_E/G_M$ is small and so are unquenching effects. Using chiral effective theory to one-loop to extrapolate the magnetic moment to the chiral limit, that the lattice results extrapolate nicely to the experimental value. The charge radius, on the other hand, is constant over the range of quark masses used in this work and therefore deviates from experiment. This is again related to the deviation observed between experiment and lattice results in the case of the charge form factor. Since the lattice size in the quenched case is large, we do not expect finite volume effects to be the reason for the discrepancy. What needs to be checked is finite lattice spacing effects and whether we are close enough to the chiral limit. The observed disagreement with experiment in the case of the charge form factor is puzzling and a study using finer lattices should follow. If one requires in addition dynamical fermions and small quark masses to be closer to the chiral limit, then such a study would require large computer resources. Unquenched configurations with pion masses down to 250 MeV on reasonably large and fine lattices will become available in the near future enabling us, using the techniques of the current work, to obtain results closer to the physical regime avoiding uncontrolled extrapolations.

ACKNOWLEDGMENTS

We would like to thank B. Orth, Th. Lippert, and K. Schilling [6] as well as C. Urbach, K. Jansen, A. Shindler, and U. Wenger [7] for providing the unquenched configurations used in this work. A. T. would like to acknowledge support by the University of Cyprus and the program "Pythagoras" of the Greek Ministry of Education. C. A. and J. W. N. would like to thank the Institute for Nuclear Physics at the University of Washington for its hospitality an partial support during the completion of this work. The computations for this work were partly carried out on the IBM machine at NIC, Julich, Germany. This work is supported in part by the EU Integrated Infrastructure Initiative Hadron Physics (I3HP) under Contract No. RII3-CT-2004-506078 and by the U.S. Department of Energy (D.O.E.) Office of Nuclear Physics under Contract No. DF-FC02-94ER40818. This research used resources of the National Energy Research Scientific Computing Center, which is supported by the Office of Science of the U.S. Department of Energy under Contract No. DE-AC03-76SF00098.

[1] M. Jones *et al.*, Phys. Rev. Lett. **84**, 1398 (2000); O. Gayou *et al.*, Phys. Rev. C **64**, 038202 (2001); Phys. Rev. Lett. **88**, 092301 (2002).
[2] H.-Y. Gao, Int. J. Mod. Phys. E **12**, 1 (2003).
[3] C. E. Hyde-Wright and K. de Jager, Annu. Rev. Nucl. Part. Sci. **54**, 217 (2004).
[4] M. Burkardt, Int. J. Mod. Phys. A **18**, 173 (2003).
[5] M. Gockeler *et al.*, Phys. Rev. D **71**, 034508 (2005).
[6] B. Orth, Th. Lippert, and K. Schilling, Phys. Rev. D **72**, 014503 (2005).
[7] C. Urbach *et al.*, Comput. Phys. Commun. **174**, 87 (2006).
[8] D. B. Leinweber and R. M. Woloshyn, Phys. Rev. D **43**, 1659 (1991).
[9] D. Dolgov *et al.* (LHP Collaboration and TXL Collaboration), Phys. Rev. D **66**, 034506 (2002).
[10] C. Alexandrou *et al.*, Phys. Rev. Lett. **94**, 021601 (2005).
[11] C. Alexandrou *et al.*, Phys. Rev. D **69**, 114506 (2004).
[12] C. Alexandrou *et al.*, Nucl. Phys. B **414**, 815 (1994).
[13] M. Albanese *et al.*, Phys. Lett. B **192**, 163 (1987).
[14] C. Morningstar and M. J. Peardon, Phys. Rev. D **69**, 054501 (2004).
[15] A. Hasenfratz and F. Knechtli, Phys. Rev. D **64**, 034504

(2001).

[16] L. Andivahis *et al.*, Phys. Rev. D **50**, 5491 (1994); R. C. Walker *et al.*, Phys. Rev. D **49**, 5671 (1994); A. F. Sill *et al.*, Phys. Rev. D **48**, 29 (1993); P. E. Bosted *et al.*, Phys. Rev. C **42**, 38 (1990); F. Borkowski *et al.*, Nucl. Phys. B **93**, 461 (1975).

[17] H. Anklin *et al.*, Phys. Lett. B **336**, 313 (1994); **428**, 248 (1998); G. Kubon *et al.*, Phys. Lett. B **524**, 26 (2002); W. Xu *et al.*, Phys. Rev. Lett. **85**, 2900 (2000); Phys. Rev. C **67**, 012201 (2003); A. Lung, Phys. Rev. Lett. **70**, 718 (1993); R. Madey *et al.*, Phys. Rev. Lett. **91**, 122002 (2003); G. Warren *et al.*, Phys. Rev. Lett. **92**, 042301 (2004); D. Rohe *et al.*, Phys. Rev. Lett. **83**, 4257 (1999); J. Bermuth *et al.*, Phys. Lett. B **564**, 199 (2003).

[18] S. Galster *et al.*, Nucl. Phys. B **32**, 221 (1971).

[19] B. D. Milbrath *et al.*, Phys. Rev. Lett. **80**, 452 (1998); Th. Pospischil *et al.*, Eur. Phys. J. A **12**, 125 (2001); V. Punjabi *et al.*, Phys. Rev. C **71**, 055202 (2005).

[20] S. Necco and R. Sommer, Nucl. Phys. B **622**, 328 (2002).

[21] S. Ando, J.-W. Chen, and C.-W. Kao, hep-ph/0602200.

[22] T. R. Hemmert and W. Weise, Eur. Phys. J. A **15**, 487 (2002).

[23] T. Bakeyer *et al.* (QCDSF-UKQCD Collaboration), Nucl. Phys. B, Proc. Suppl. **128**, 82 (2004).